Optics & Laser Technology 175 (2024) 110882

Contents lists available at ScienceDirect

Optics and Laser Technology

journal homepage: www.elsevier.com/locate/optlastec

Optical fiber probe based on LSPR for the detection of pesticide Thiram

Amin Moslemi [a], Lucia Sansone [b,*], Flavio Esposito [a], Stefania Campopiano [a], Michele Giordano [b], Agostino Iadicicco [a,*]

[a] Department of Engineering, University of Naples "Parthenope", 80143 Naples, Italy
[b] Institute for Polymers, Composites, and Biomaterials, National Research Council of Italy, IPCB-CNR, 80055 Portici, Italy

ARTICLE INFO

Keywords:
Fiber optic sensors
Optical fiber sensors
Gold nanoparticles
Localized surface plasmon resonance
Chemical sensors
Biosensors

ABSTRACT

This article introduces an innovative sensor designed to explore the localized surface plasmon resonance (LSPR) effect using optical fiber technology for the detection of pesticide Thiram. The proposed configuration consists of an etched silica multimode optical fiber coated with gold nanoparticle (AuNP) layers able to modulate the reflected signal. What sets this sensor apart is its ability to stimulate LSPR modes for single AuNPs, i.e. single layer, and aggregation states of nanoparticles or multilayer. This capability has been demonstrated through both numerical simulations and experimental results. Furthermore, the device has been applied to detect a specific pesticide, Thiram, serving as an illustrative example of chemical sensing, for concentrations within 0.1–100 μM, and achieving a low limit of detection (LOD) below 5 nM.

1. Introduction

The widespread integration of optical fiber sensors for chemical and biological applications is noteworthy, showcasing significant potential to supersede conventional and cumbersome sensing devices. Their compact form, flexibility, and resistance to electromagnetic interference position them as promising candidates for diverse applications, enabling remote measurements in areas such as temperature, pressure, and refractive index (RI) monitoring, along with biomarker and chemical compound quantification [1–6].

Diverse optical detection techniques exist, each requiring specific geometries, materials, and equipment for effective implementation [7–12]. Plasmonic methods, particularly surface plasmon resonance (SPR), stand out for their swift, label-free, and real-time sensitivity. In this mechanism, an interplay and energy exchange occurs between incident light photons and electrons on a metal surface, resulting in their collective oscillation. SPR unfolds at the interface between a dielectric and a metal nano-film, leading to the propagation of surface plasmon polaritons [13–19].

Gold nanoparticles (AuNPs) are preferred for chemical and biosensor applications due to their exceptional features, including excellent compatibility, intense light scattering/absorption, high surface area to volume ratios, selective interoperability through electrostatic interaction, stable structure, and non-toxicity. Additionally, AuNPs are harnessed for the excitation of the localized surface plasmon resonance (LSPR) phenomenon, extensively explored in recent sensing platforms owing to its significant advantages [19–26]. This phenomenon in metallic nanostructures is linked to the resonance of free-electron waves in metal, where incident light resonates with the oscillations of surface electrons at an excitation frequency, resulting in the collective oscillation of surface plasmons, known as an LSPR mode. LSPR offers a compact, label-free, highly sensitive, and stable biosensing approach for detecting biological components that are relevant to the health of mankind and the environment [27–31].

In this context, Thiram, a commonly used fungicide in agriculture, poses significant health risks due to its excessive use, leading to issues such as skin and mucosal irritation, and even organ damages. Therefore, detecting Thiram residues in the environment is crucial. Traditional detection methods, such as ion mobility spectrometry and high-pressure liquid chromatography, rely on expensive and intricate equipment [32,33]. Currently, colorimetric detection methods for thiram residues based on noble metal nanoparticles have been developed [34,35]. Gold, silver, and copper nanoparticles, chemically modified, are utilized to determine thiram concentration through their distinctive LSPR effect. However, many of these methods struggle to achieve a satisfactory limit of detection (LOD), or their preparation procedures are excessively complex. For example, Ke Lui et al. [36] utilized the LSPR effect of aggregated AuNPs in a UV–VIS spectrometer for the sensitive detection of Thiram, achieving a remarkable limit of detection (LOD) of 0.04 μM. In another investigation, Jigneshkumar V. Rohit et al. [37] employed the

* Corresponding authors.
E-mail addresses: lucia.sansone@ipcb.cnr.it (L. Sansone), agostino.iadicicco@uniparthenope.it (A. Iadicicco).

https://doi.org/10.1016/j.optlastec.2024.110882
Received 30 January 2024; Received in revised form 6 March 2024; Accepted 11 March 2024
Available online 20 March 2024

same method with silver nanoparticles in a UV–VIS spectrometer and achieved a LOD of 2.81 μM [38,39]. Additionally, the Surface Enhanced Raman Scattering (SERS) phenomenon has been used for Thiram detection, as demonstrated by Lili Kong et al. [40], who achieved a detection limit of 2 ppm. In another investigation conducted by Grégory Barbillon et al. [41], assembled Au/ZnO nano-urchins were employed as SERS substrates, achieving an impressive LOD of 10 pM. Despite these methods being able to achieve low LODs, most of them could be only performed in a laboratory using cumbersome and expensive equipment.

In this work, a fiber optic probe utilizing localized surface plasmon resonance is reported. The probe has been designed with a 43 nm AuNP layer deposited along the surface of an etched and tip-mirrored multimode optical fiber (MMF). The reflected signal of the device is thus modulated by the AuNPs extinction spectrum. This configuration has been employed to detect Thiram concentration in water by monitoring the wavelength shift of LSPR, due to the chemical affinity between AuNPs and the pesticide. Along with the simplicity of the fiber probe and the read-out setup, a low LOD down to 1 nM has been achieved.

2. Materials and methods

2.1. Chemicals

Tetrachloroauric acid ($HAuCl_4 \cdot 3H_2O$, 99 %), trisodium citrate (99 %), distilled water, Piranha solution (mixture of H_2SO_4 and H_2O_2 7:3 v/v); (3-Aminopropyl) triethoxysilane (APTES) in acetone (5 % w/w), Tetramethyl thiuram disulfide (Thiram) and used without further purification have been purchased from Merck Life Science (Milano, Italy). A solution of Thiram in deionized water has been prepared as a stock solution of 10^{-5} M and different concentrations have been prepared by serial dilution techniques (10^{-5} M, 10^{-6} M, 10^{-7} M, and 10^{-8} M).

2.2. Synthesis and characterization of AuNPs

The synthesis of citrate-stabilized AuNPs based on the single-phase aqueous reduction of tetrachloroauric acid by sodium citrate, was initially developed by Turkevich et al. in 1951 and further refined by Frens et al. [42]. Following this strategy, it is possible to control the size of AuNPs typically from about 5 nm to 150 nm by varying the reaction conditions (sodium citrate to gold salt ratio, solution pH, and solvent). Specifically, in our case we have produced AuNPs using a seeded growth strategy for the synthesis of size- and shape-controlled large citrate-stabilized AuNPs based on the classical Turkevich/Frens reaction system, as reported in the following.

In a 250 mL three-necked round-bottomed flask, a solution comprising 2.2 mM sodium citrate in distilled water (150 mL) has been heated using a heating mantle for 15 min with vigorous stirring. To prevent solvent evaporation, a condenser has been also utilized. Upon the initiation of boiling, 1 mL of a 25 mM $HAuCl_4$ solution has been introduced. The solution exhibited a color transition from yellow to bluish-grey and then has been settled into a soft pink hue within 10 min. Immediately following the synthesis of the Au seeds, and within the same reaction vessel, the reaction has been cooled until the solution temperature reached 90 °C. Subsequently, 1 mL of a 25 mM $HAuCl_4$ solution has been injected, and after 30 min, the reaction is concluded. This entire process has been repeated twice. Following this, the sample has been diluted by extracting 55 mL of the solution and adding 53 mL of ultra-pure water and 2 mL of a 60 mM sodium citrate solution. The resulting solution has been used as the seed solution, and this entire process has been reiterated five times, as depicted in Fig. 1.

UV–Vis absorption spectra of AuNPs has been acquired using an Agilent Cary 60 UV/Vis spectrophotometer and quartz cuvettes. To prevent saturation, dispersion samples have been adequately diluted in deionized water at a ratio of 1:8 v/v. Fig. 2(A) depicts the visible (VIS) spectrum of AuNPs, showcasing a plasmon resonance band at 525 nm. As the wavelength is directly connected to the NP size, the absorbance peak wavelength can be moved on demand by varying the reaction conditions: it can be tuned from about 520 nm to 575 nm when the AuNP diameter changes from 20 nm to 100 nm [43].

To investigate the morphology of AuNPs, transmission electron microscopy (TEM) experiments have been carried out using a TEM FEI Tecnai G12 Spirit Twin, equipped with a LaB6 emission source (120 kV) and paired with a CCD camera Fei Eagle 4 K (Japan). For TEM specimen preparation, a diluted suspension of AuNPs has been placed on a carbon-coated copper grid, air-dried, and introduced into the electron microscope chamber. The inset in Fig. 1 shows a representative AuNPs TEM image. Statistical image analysis has been performed by Image J software. The AuNPs are characterized by a spherical shape and the size distribution is plotted in Fig. 2(B) exhibiting an average diameter of 43.1 ± 8.8 nm.

3. Numerical analysis

For the aim of the work, the optical absorption band of nanoparticles in both individual and aggregated groups has been calculated, to comprehend the experimental reflection spectrum. In this segment, the initial focus is on investigating the optical reaction of a single nanoparticle. Subsequently, the impact of aggregation is examined. In the subsequent phase, diverse combinations of aggregation levels are simulated, examining both single AuNPs and aggregations. Moreover, simulations are conducted with different solutions, each featuring varied participation weights of aggregation levels. This aims to unravel the behavior associated with increasing aggregation concerning the absorption spectrum.

The structural behavior is simulated using commercial software based on the Finite Element Method (FEM). At the simulation core lies

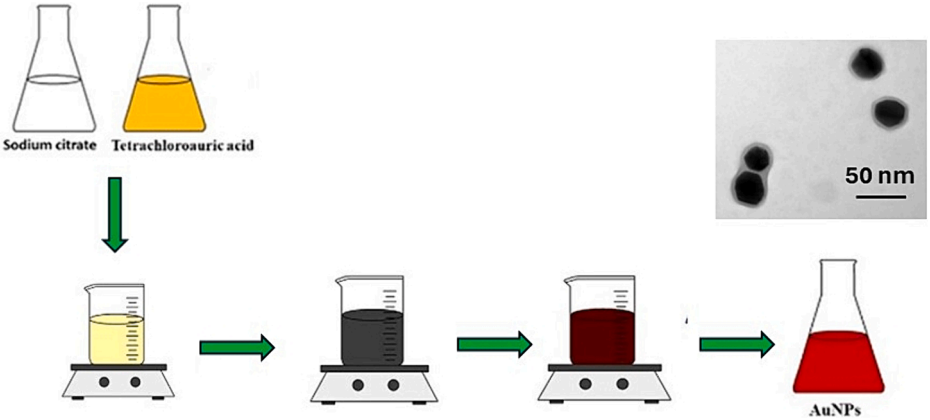

Fig. 1. Synthesis of gold nanoparticles and in inset TEM image of the same [42].

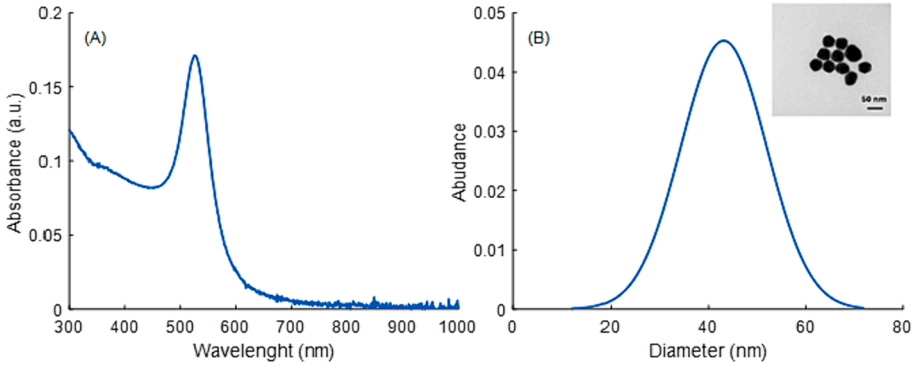

Fig. 2. (A) UV spectrum of AuNPs in solution; (B) Size distribution of AuNPs, in inset a representative TEM image of AuNPs.

either a singular or an aggregate of nanoparticles, each possessing a 50 nm diameter (as an exemplary). In the initial stage, the attention is focused on a single nanoparticle enveloping this central element in a 200 nm thick dielectric layer (with a refractive index equal to the one of water, i.e., 1.333), followed by another 200 nm dielectric layer serving as a perfectly matched layer (PML), i.e. ensuring a good compromise between computational time and accuracy, as reported in Fig. 3(A). The purpose of the PML is to establish an infinite dielectric environment around the gold structure. This configuration ensures that incident light is not reflected toward the gold structure. The incoming light is planar in the z-direction, ranging from -z to + z, and polarized in the x-direction. The power of the illumination is maintained at 1 W/m^2. In Fig. 3(B), the electric field distribution on the surface of the gold nanoparticle at the wavelength of $\lambda = 480$ nm is depicted [12,44].

Utilizing the FEM analysis, the heat losses as a function of the wavelength of exciting light are computed enabling the characterization of the absorption spectrum plotted with the red line in Fig. 4(A). As expected, a single absorption peak at approximately $\lambda = 535$ nm is observed when the surrounding medium is water, in good agreement with the literature [45,46] and data in Fig. 2(A). The absorption wavelength is strongly connected to AuNP size [43]. Moreover, Fig. 4(A) plots the absorption spectra of the single AuNP by changing the refractive index of the surrounding medium (SRI), observing a redshift in the absorption band peak with SRI. The sensitivity is quantified by tracking the resonance wavelength peak versus SRI as plotted in Fig. 4 (B) with a determined value of 200 nm/RIU (refractive index unit) in the range of SRI = 1.33–1.35. According to our simulations, as well as literature, nanoparticles within the size range of 50 nm exhibit the highest sensitivity [47,48].

Different aggregation states are explored in the subsequent simulation phase, featuring groups of 2 and 3 nanoparticles, each with a 50 nm diameter in a water environment. Fig. 5(A) plots the 2 nanoparticles (2-NP) case aligned along the x-axis (in xy plane). Light propagation and polarization are kept unchanged, indicating that two nanoparticles have aggregated side by side in a linear arrangement orthogonal to the direction of light propagation. The corresponding absorption spectrum is plotted in Fig. 5(B) with black line exhibiting a single peak, i.e., the absorption band closely resembles that of a single nanoparticle, as depicted in Fig. 4(A) and the peak is at the wavelength of 560 nm.

Further, Fig. 5(B) also plots the absorption spectra of 2-NP with rotation along the y-axis, with different angles, i.e., 30°, 45°, 60° and 90°. The absorption spectrum significantly changes as a function of 2-NP rotation angle, exhibiting two peaks with different amplitudes in most of the cases. Specifically, as the rotation angle increases, the overall size along z-axis (light propagation axis) increases. The simplest interpretation of the phenomena links the peak at lower wavelengths to the size of the single NP whereas the peaks at higher wavelengths are attributed to larger size of 2-NP aggregates along z-axis (light propagation axis), as effect of the rotation. As experimental conditions involve the amalgamation of absorption bands from several nanoparticles at different incident angles, the brown line representing the average spectrum across various incident angles is also reported.

Moreover, a cluster of three nanoparticles has been arranged in a close-packed triangular configuration in the xy plane as can be observed in Fig. 6(A). The corresponding absorption spectrum is plotted in Fig. 6 (D) using black curve and, as expected, a single peak is observed.

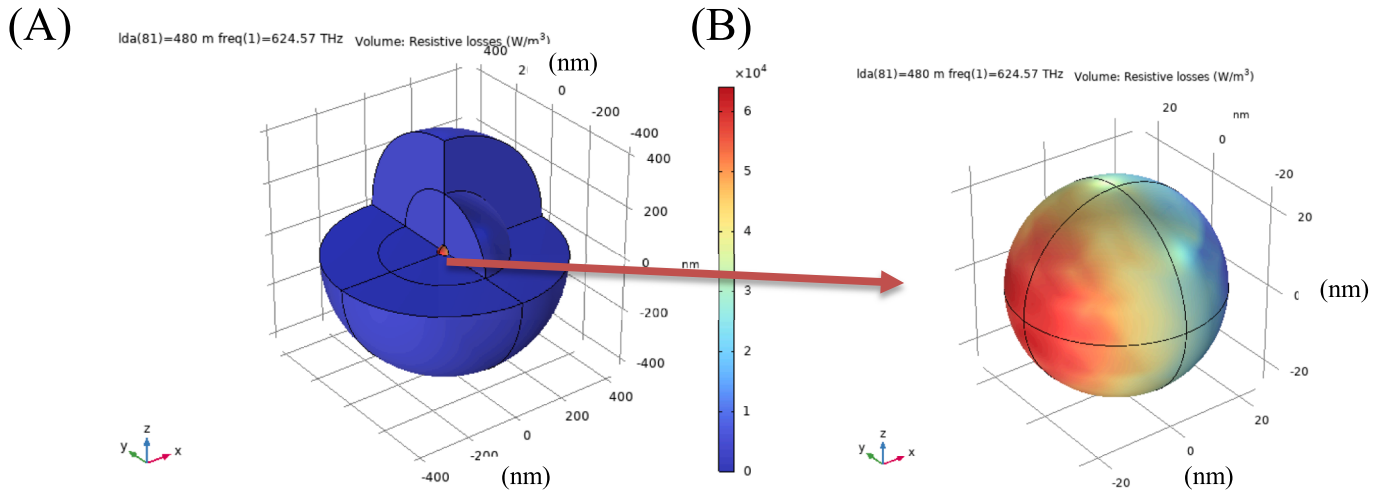

Fig. 3. Schematic of the simulation environment: (A) Several layers including the gold structure, dielectric layers, and the PML; (B) The distribution of the electric field surrounding each gold nanoparticle.

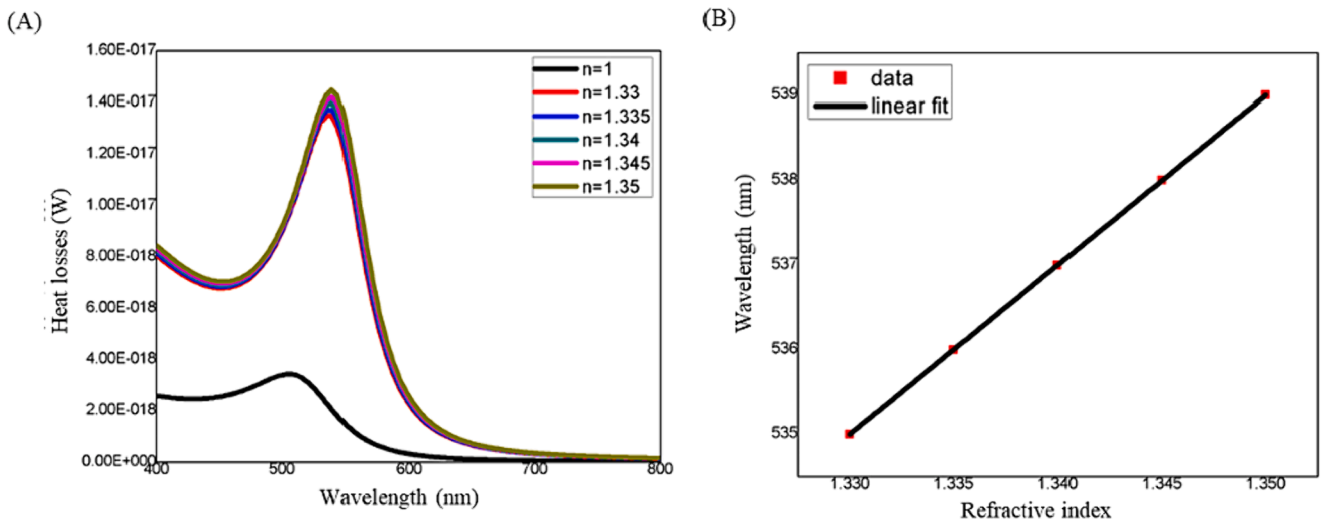

Fig. 4. (A) The absorption spectra of a single AuNP at different surrounding refractive index; (B) Resonance wavelength of the absorption band peak versus surrounding refractive index.

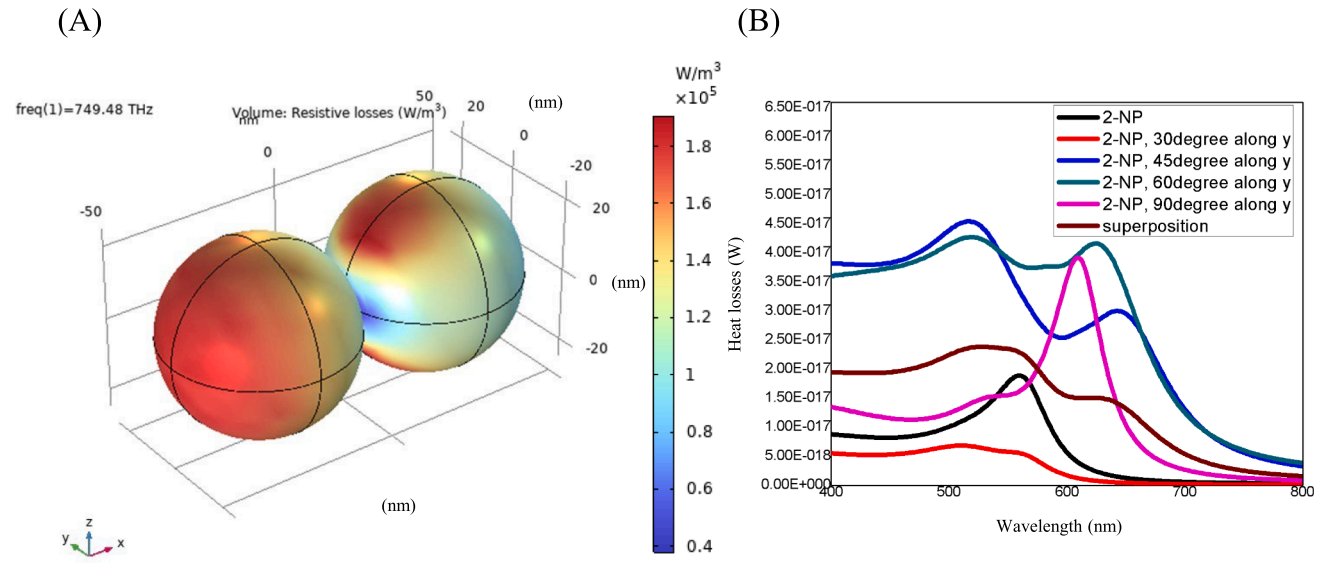

Fig. 5. Simulation of two nanoparticles: (A) spatial configuration and electric field distribution; and (B) absorption spectra for various configurations and the superposition of these spectra.

Subsequently, the structure shown in Fig. 6(B) have been rotated, as depicted in both Fig. 6(B) and (C), and related absorption spectra are plotted in Fig. 6(D). Similarly to the previous case, the spectra significantly change as a function of the angle between the AuNP plane and light propagation. In the case of Fig. 6(B), three peaks are observed (red line), with two nanoparticles aligned in a single line orthogonal to the direction of light propagation and an additional NP positioned above them. As a result, when light interacts with this structure, it encounters three different scenarios, leading to the presence of three peaks in the spectrum. It's worth noting that the first peak is related to a single nanoparticle. Finally, the blue line represents a spectrum associated with the structure in Fig. 6(C). In this arrangement, two nanoparticles are stacked on top of each other in a single line along the z-axis, with a third NP positioned on the side of both. This configuration exhibits two peaks, similar to the blue and green lines in Fig. 5(B), which represent two NPs positioned adjacent to each other but not oriented orthogonally to the direction of light propagation.

In summary, the number of peaks in the spectrum is directly related to the number of distinct scenarios that can be perceived by incident light. Additionally, the initial peak related to a single nanoparticle remains consistent across all superposition configurations.

However, in real-world conditions taking into consideration colloidal AuNPs solutions or, more specifically, AuNPs layer deposited on the surface of transducer devices, the absorption spectrum displayed is a composite of diverse contributions arising from the AuNPs single and multi-layer regime. Hence, as a simplified scenario, we consider various solutions with different ratios of single nanoparticles, clusters of two, and clusters of three nanoparticles simulated. The absorption spectra for these configurations have been calculated, incorporating participation weights as specified in Table 1. Consequently, Fig. 7 illustrates that the superposition of different levels of aggregation leads to two main peaks. Based on the previous observations from Figs. 5 and 6, it is evident that in all the solutions listed in Table 1, individual nanoparticles are consistently present. Hence, the behavior of single nanoparticles, i.e. single layer, contributes significantly to the absorption spectrum, representing the initial prominent peak. It is important to note that the final

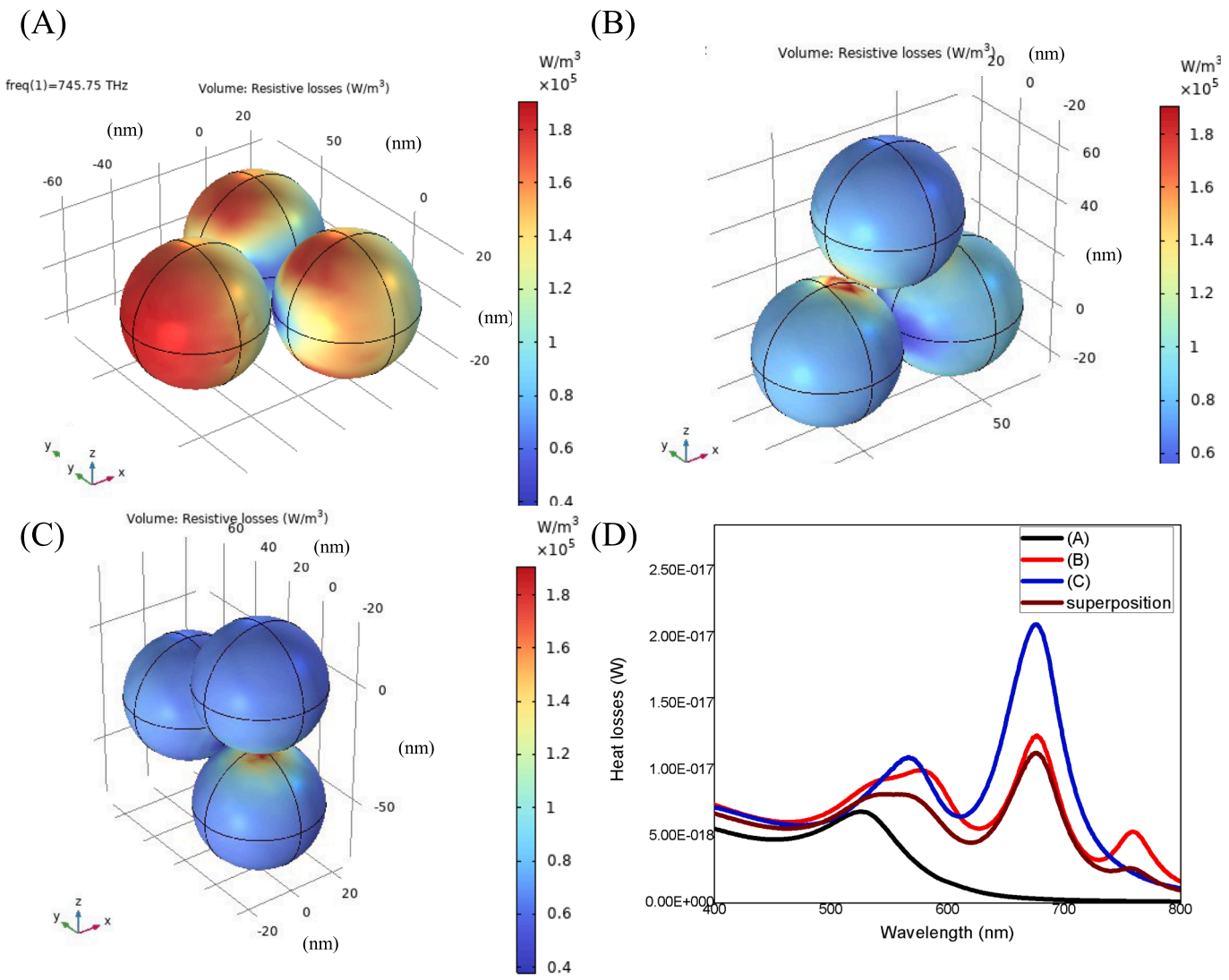

Fig. 6. Simulation of three nanoparticles: (A), (B), (C) three different spatial configuration and related electric field distributions; (D) absorption spectrum for the various configurations and the superposition of these spectra.

Table 1
Properties of the calculated solutions.

aggregation state	s1	s2	s3	s4
single nanoparticle	33.33 %	50 %	25 %	25 %
superposition of 2 NPs	33.33 %	25 %	50 %	25 %
superposition of 3 NPs	33.33 %	25 %	25 %	50 %

spectrum represents an average of all these behaviors, ultimately leading to the presence of two main absorption bands. Notably, as the participation weight of higher aggregation level clusters increases, the second peak becomes more prominent, showing a heightened redshift.

Even if in this analysis a limited number of aggregations and orientations are considered, it permits understanding the experimental spectra in the next section.

3.1. Design and fabrication of optical fiber probe

The optical probe considered in this work is mainly composed of an etched fiber working in reflection (or single-ended) mode, as schematically reported in Fig. 8(A). In this approach, a few centimeters at the end of a silica multimode fiber are etched using hydrofluoric acid until the cladding is completely removed. In this scenario, the light guided

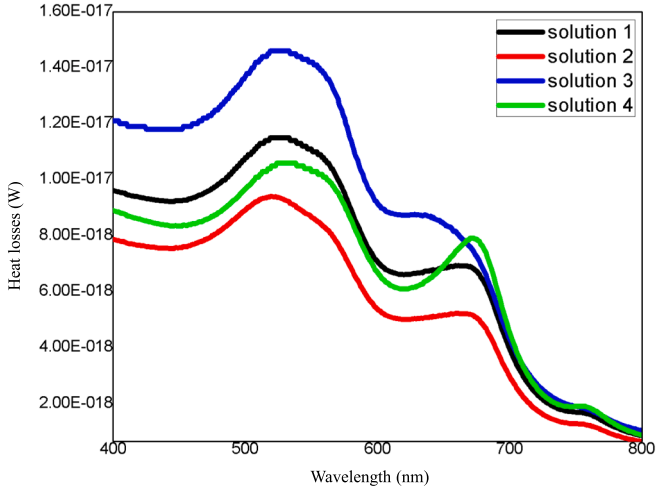

Fig. 7. Numerical absorption spectra related to four distinct combinations of single, two, and three nanoparticles. Details of the solutions are reported in Table 1.

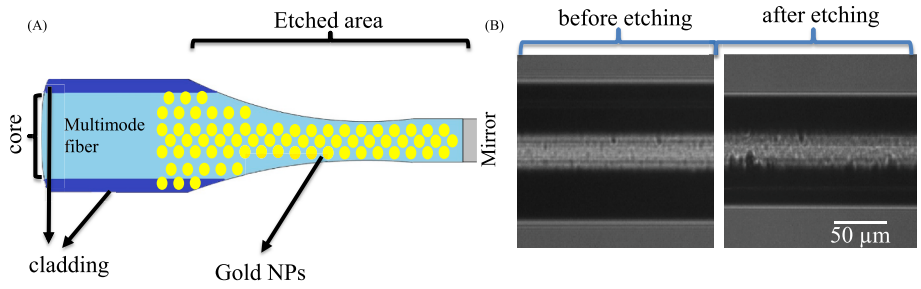

Fig. 8. (A) Schematic of the fiber probe. (B) Differences in diameter between etched and non-etched fibers.

into the fiber escapes into the surrounding environment as an evanescent wave. The evanescent waves are highly sensitive to the dielectric characteristics of the surrounding environment. The light is then reflected from a mirror integrated into the fiber end, enabling the reflection mode configuration. Moreover, gold nanoparticles with a diameter of 43 nm are deposited along the surface of the etched fiber. These nanoparticles absorb a specific portion of the light spectrum based on their size, configuration, and the refractive index of the surrounding area. If the refractive index undergoes any changes, the reflected spectrum of the fiber probe will alter in terms of wavelength shift and amplitude.

Specifically, the multimode fiber FG105LCA by Thorlabs with a 105/125 µm core/cladding diameter has been chosen. For the aim of the work, the acrylate coating of the fiber has been removed using a stripper, and 5 cm of the stripped region has been immersed in a 24 % hydrofluoric acid (HF) solution for 25 min, followed by a thorough wash with deionized water. Based on image processing analysis from Fig. 8(B), the diameter of the etched fiber is approximately 99 µm. This indicates the complete removal of the cladding and a small portion of the core, allowing evanescent waves to propagate outward.

The subsequent stage involves the linking of AuNPs on the etched fiber surface. To make it as stable as possible the etched fiber surface has been properly functionalized by a sequence of exposure to piranha solution and APTES. Briefly, the etched portion of the fiber has been first immersed in a piranha solution for an hour to facilitate the formation of hydroxyl groups, followed by a thorough rinsing with water. Following this, the fiber tip has been precisely cleaved and mirrored through Tollen's reaction to develop a single-ended probe. Following this step, the fiber has been immersed in APTES (5 % w/w) for two hours to have silanization of the surface, then cleaned with acetone and left to air-dry overnight. Finally, the fiber has been submerged in a solution containing gold nanoparticles (43 nm, 1 mM) for 4 h and allowed to air-dry throughout the night [1,49]. There is a self-organization of AuNPs on different orientations of self-assembled APTES molecules on fiber substrate.

The spectral analysis during fabrication and characterization has been carried out by a standard and cheap setup. The light from a fiber optics-coupled white light source (Avantes AvaLight-HAL-S-Mini) is transmitted to the transducer through a multimode optical fiber coupler, and the resultant reflection spectrum is directed to a spectrometer (Ocean Optic HR2000+), as illustrated in Fig. 9(A). The setup reference has been taken considering the precisely cut multimode fiber. After establishing the reference for the setup, the probe has been spliced to the cleaved etched fiber.

The depicted Fig. 9(B) shows the transducer reflected spectrum after the deposition of gold nanoparticles, taken when the device is in the air, concerning the reflected spectrum of mirrored fiber before AuNPs. This spectrum exhibits two deeps located at 545 nm and 733 nm, respectively. According to the numerical analysis, the first deep in the absorption spectrum is attributed to the absorption band of a single layer. This corresponds to a scenario where evanescent waves interact orthogonally with the fiber surface and the first deep results from the presence of a uniform layer of nanoparticles on the fiber surface. Conversely, the second deep in the spectrum is associated with multilayer configurations. In this case, the second deep arises from clusters of nanoparticles with varying angles relative to the propagation direction of the evanescent waves. Due to the high number of clusters, their superposition creates a smooth second deep in the absorption band.

After fabrication, a stability test has been conducted to assess whether the nanoparticles are well-grafted to the fiber surface. The adopted procedure consists of immersion of the fiber probe in water with subsequent extraction and drying. Fig. 10(A) plots the spectra of the same sample related to successive immersions in water showing very good repeatability. Therefore, subsequent experimental steps do not indicate any changes in the spectrum due to mechanical alterations in the nanoparticle structure.

4. SRI characterization

The sensor sensitivity has been evaluated concerning the variations

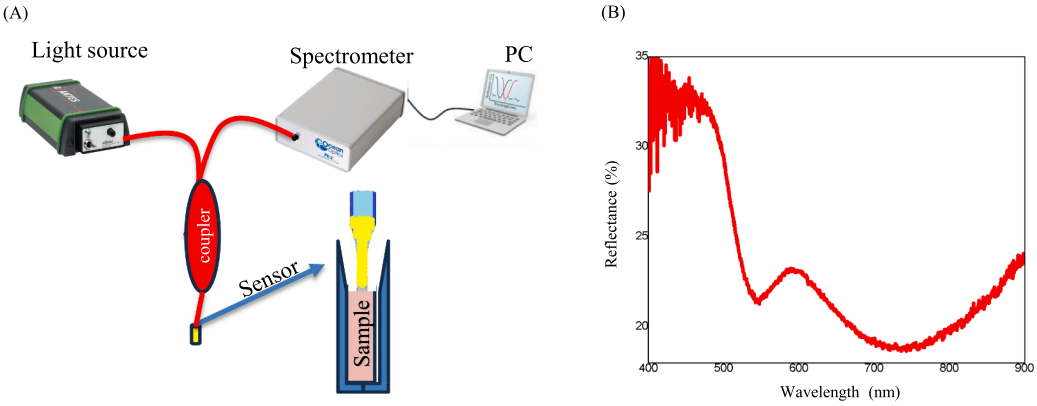

Fig. 9. (A) Schematic of the optoelectronic readout setup. (B) Reflected spectrum of the fiber device taken in air.

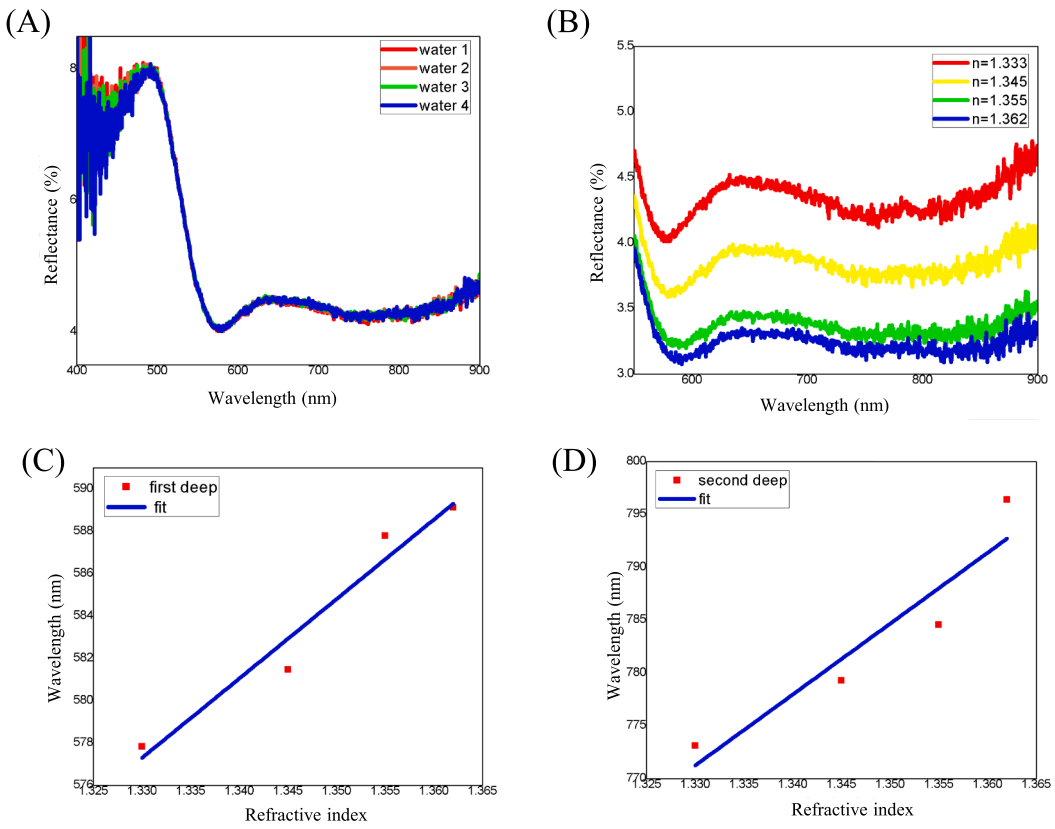

Fig. 10. (A). Reflection spectra related to subsequent immersion in water; (B) Reflection spectra under varying surrounding refractive indices; (C) and (D) resonance wavelength versus surrounding refractive index for first and second deep, respectively.

in the surrounding medium refractive index. In this assessment, diverse solutions have been created by combining deionized water and glycerin in varying proportions. The specific refractive index of each solution has been subsequently determined using an Abbe refractometer (with a resolution of $2\bullet10^{-4}$). Hence, the fiber probe has been completely immersed in each solution and washed with deionized water after each immersion. Notably, both the first and second peaks demonstrate a redshift with the surrounding refractive index, as illustrated in Fig. 10 (B). Fig. 10(C) and (D) depict the shift of first and second resonant wavelengths versus surrounding refractive index, respectively, exhibiting high sensitivity of 433 nm/RIU and 581 nm/RIU by considering a linear trend in the range 1.33–1.36, respectively [50,51].

5. Thiram detection

Thiram pesticide has functional groups such as amine of thiol which can strongly bind to Au nanoparticles. The interaction between thiram and gold nanoparticles alters the surface electrical properties,

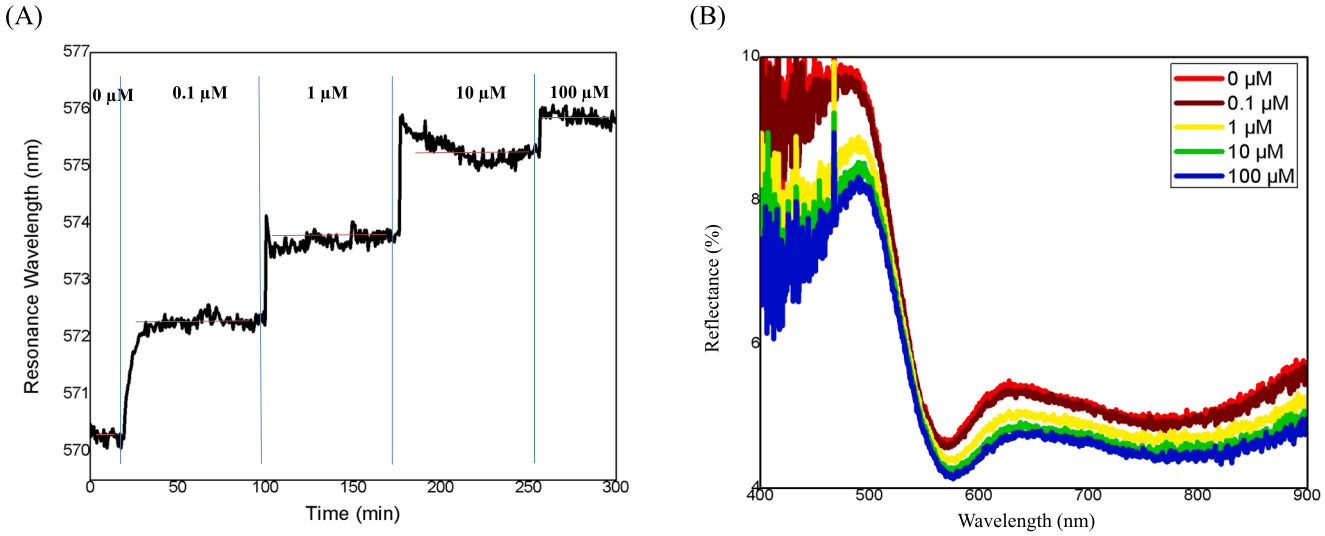

Fig. 11. (A) Sensorgram as function of the Thiram concentration: the horizontal red lines represent the average values of the attenuation band after stabilization and the vertical blue lines indicate the time when solutions have been changed; (B) Reflection spectra at different Thiram concentrations.

influencing surface plasmon resonance [52].

Here, the fiber probe prepared according to previously reported steps has been employed to measure variations in Thiram concentration in water solutions, within 0.1–100 μM. It is worth noting that, the variation of the refractive index of the thiram solutions is expected to be less than $2\bullet10^{-4}$ since no difference is measured by the Abbe refractometer. Moreover, due to the limited visibility of the second deep in the reflection spectrum, the sensing of Thiram is focused solely on tracing the first attenuation band. This approach ensures a more accurate and reliable assessment of Thiram concentration, emphasizing the distinctive features within the primary absorption region of the spectrum.

The real-time response in terms of resonance wavelength of the absorption peak, when the fiber probe is sequentially immersed in different solutions with increasing Thiram concentration, is plotted in Fig. 11(A). Here, the probe has been initially immersed in pure water (zero concentration) for 20 min. The sensorgram has been achieved by recording data each 30 s. According to the plot, an observable redshift in the attenuation band occurs with an increase in the concentration of Thiram. Fig. 11(B) depicts the reflection spectra of the probe at various concentrations after achieving spectral stability, where good visibility of the spectral features can be observed during the whole experiment.

Subsequently, the calibration curve of the sensor has been obtained and reported in Fig. 12 using a semi-logarithmic scale, showing the resonance wavelength shift concerning Thiram concentration. Here, the resonance wavelength is reported concerning the initial value of the baseline (at zero concentration). The mean value and two times the associated standard deviation for 60 subsequent measurements as error bars are displayed for each experimental point data. The fitting of the experimental data is also presented using dashed curves, employing the Logistic function. The expression of the Logistic function is particularly advantageous when expressed in terms of wavelength shift (Δλ), as detailed in the literature [53,54]:

$$\Delta\lambda = \Delta\lambda_{MAX} \bullet \left[\frac{\left(\frac{x}{x_0}\right)^p}{1+\left(\frac{x}{x_0}\right)^p}\right] \quad (1)$$

$\Delta\lambda_{MAX}$ represents the disparity between the asymptotes of the sigmoidal curve, serving as an indicator of the dynamic signal change, commonly referred to as the dynamic range. The parameter x_0 denotes the analyte concentration value at which the wavelength shift equals 50 % of the dynamic range. Additionally, the coefficient p is associated with the slope of the sigmoidal curve $x = x_0$. In essence in Eq. (1), $\Delta\lambda_{MAX} = 5.58$ nm is anticipated to vary proportionally to the sensitivity of the sensor, where both $x_0 = 0.439\ \mu M$ and $p = 0.577$ are contingent on the binding interaction between Thiram and AuNPs.

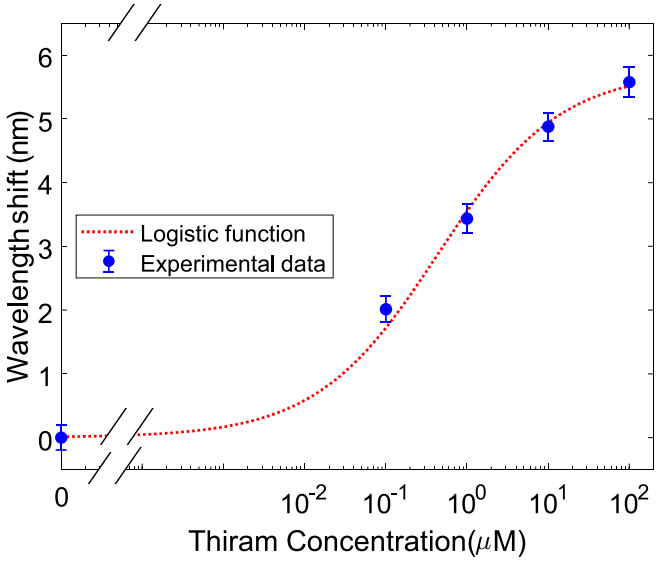

Fig 12. Semi-log calibration curve of the sensor for Thiram detection.

By the literature [55], several parameters of interest can be extracted from the calibration curve to evaluate the sensor performance. Notably, the limit of detection (LOD) stands out as one of the most crucial parameters, which is defined as the analyte concentration corresponding to the signal variation associated with the zero concentration of the analyte (blank measurement) plus three times its standard deviation. The maximum standard deviation for this measurement is 0.12 nm, so by considering the Logistic function data (red line in Fig. 12) the computed limit of detection is lower than LOD = 5 nM. The performance of the sensor is compared with existing literature in Table 2: it can be observed that the LOD is lower if compared to UV–VIS-based methods proposed in, anyway it is higher than that achieved by SERS-based methods, typically in the range of a few pM [34,56–61]. However, the advantage of this method lies in its significantly lower cost and portability, making this technology a valid candidate in many practical sensing scenarios.

6. Conclusion

In this work, a fiber optic probe has been meticulously designed, featuring an etched silica multimode fiber coated with 43 nm AuNPs. The resulting reflection spectrum exhibits two distinct attenuation bands. The sensitivity of the attenuation bands to changes in the surrounding medium refractive index has been quantified, revealing values of 433 nm/RIU and 581 nm/RIU for the first and second attenuation bands, respectively. Notably, the second attenuation band exhibits higher sensitivity, emphasizing its potential significance in applications involving RI variations. Additionally, the behavior of aggregated nanoparticles with varying levels of isolation, including different participation weights for each aggregation level, has been thoroughly investigated by numerical simulations. The simulations aim to provide insights into the optical properties and responses of both individual and clustered nanoparticles under different conditions. These findings confirm the accuracy of the simulations in capturing the optical characteristics of the fabricated probe.

In the subsequent stage of experimentation, the developed device has been employed for sensing concentration changes in a chemical component, specifically Thiram pesticide. Thiram is known to exhibit a natural reactivity with gold nanoparticles. The utilization of the fabricated fiber optic probe has successfully demonstrated its capability to sense and monitor concentration changes in response to the presence of Thiram, showcasing the practical applicability of the devised chemical sensing platform. One notable advantage of the presented sensor is its simplicity and cost-effectiveness compared to SERS-based methods, and it offers a lower LOD compared to UV–VIS-based methods. This makes it a more accessible alternative when compared to other detection methods.

CRediT authorship contribution statement

Amin Moslemi: Writing – original draft, Validation, Methodology, Investigation. **Lucia Sansone:** Writing – review & editing, Resources,

Table 2
Comparison of the sensor performance with existing literature.

Configuration	Range	LOD	Ref.
UV–VIS	2.5–20 μM	40 nM	[37]
LC-MS	0.01–0.1 mg/kg	5 nM	[60]
SERS	1 nM-10 μM	1 nM	[61]
AuNPs-CTAB spectrophotometry	0.2–10 μM	170 nM	[34]
Etched MMF with AuNPs	0.1–100 μM	5 nM	This work

Investigation. **Flavio Esposito:** Writing – review & editing, Investigation. **Stefania Campopiano:** Supervision, Conceptualization. **Michele Giordano:** Supervision, Conceptualization. **Agostino Iadicicco:** Writing – review & editing, Supervision, Conceptualization.

Declaration of competing interest

The authors declare that they have no known competing financial interests or personal relationships that could have appeared to influence the work reported in this paper.

Data availability

Data will be made available on request.

Acknowledgements

This work was supported by the Italian Ministry of University and Research through the project "Monitoring of honey Bee immunomodulation and resilience to stress factors by Fiber Optic technology" (MoBeeFO) CUP I53D23000390006 under PRIN 2022 grant. The work of Flavio Esposito was supported by the D.M. 1062/2021 - FSE REACT EU - PON Ricerca e Innovazione 2014-2020 - Azione IV.4 "Dottorati e contratti di ricerca su tematiche dell'innovazione" under contract nr. 41-I-15372-1 CUP I65F21001200001.

References

[1] M.S. Soares, M. Vidal, N.F. Santos, F.M. Costa, C. Marques, S.O. Pereira, C. Leitão, Immunosensing based on optical fiber technology: recent advances, Biosensors (basel) 11 (2021) 305, https://doi.org/10.3390/bios11090305.
[2] J. Lu, Y. Yu, S. Qin, M. Li, Q. Bian, Y. Lu, X. Hu, J. Yang, Z. Meng, Z. Zhang, High-performance temperature and pressure dual-parameter sensor based on a polymer-coated tapered optical fiber, Opt. Exp. 30 (2022) 9714, https://doi.org/10.1364/OE.452355.
[3] I. Hernandez-Romano, D. Monzon-Hernandez, C. Moreno-Hernandez, D. Moreno-Hernandez, J. Villatoro, Highly sensitive temperature sensor based on a Polymer-coated microfiber interferometer, IEEE Photon. Technol. Lett. 27 (2015) 2591–2594, https://doi.org/10.1109/LPT.2015.2478790.
[4] S. Choudhary, F. Esposito, L. Sansone, M. Giordano, S. Campopiano, A. Iadicicco, Lossy mode resonance sensors in uncoated optical fiber, IEEE Sens J 23 (2023) 15607–15613, https://doi.org/10.1109/JSEN.2023.3280675.
[5] F. Esposito, A. Srivastava, L. Sansone, M. Giordano, S. Campopiano, A. Iadicicco, Label-free biosensors based on long period fiber gratings: a review, IEEE Sens J 21 (2021) 12692–12705, https://doi.org/10.1109/JSEN.2020.3025488.
[6] G. Lopes, N. Cennamo, L. Zeni, R. Singh, S. Kumar, A.J.S. Fernandes, F. Costa, S. O. Pereira, C. Marques, Innovative optical pH sensors for the aquaculture sector: comprehensive characterization of a cost-effective solution, Opt Laser Technol 171 (2024) 110355, https://doi.org/10.1016/j.optlastec.2023.110355.
[7] H.C. Gomes, X. Liu, A. Fernandes, C. Moreirinha, R. Singh, S. Kumar, F. Costa, N. Santos, C. Marques, Laser-induced graphene-based fabry-pérot cavity label-free immunosensors for the quantification of cortisol, Sensors and Actuators Reports 7 (2024) 100186, https://doi.org/10.1016/j.snr.2024.100186.
[8] R. Singh, Z. Wang, C. Marques, R. Min, B. Zhang, S. Kumar, Alanine aminotransferase detection using TIT assisted four tapered fiber structure-based LSPR sensor: from healthcare to marine life, Biosens Bioelectron 236 (2023) 115424, https://doi.org/10.1016/j.bios.2023.115424.
[9] X. Liu, R. Singh, G. Li, C. Marques, B. Zhang, S. Kumar, WaveFlex biosensor-using novel tri-tapered-in-tapered four-Core fiber with multimode fiber coupling for detection of aflatoxin B1, J. Lightwave Technol. 41 (2023) 7432–7442, https://doi.org/10.1109/JLT.2023.3301069.
[10] M.S. Soares, L.C.B. Silva, M. Vidal, M. Loyez, M. Facão, C. Caucheteur, M.E. V. Segatto, F.M. Costa, C. Leitão, S.O. Pereira, N.F. Santos, C.A.F. Marques, Label-free plasmonic immunosensor for cortisol detection in a D-shaped optical fiber, Biomed Opt Express 13 (2022) 3259, https://doi.org/10.1364/BOE.456253.
[11] C.A.F. Marques, G.-D. Peng, D.J. Webb, Highly sensitive liquid level monitoring system utilizing polymer fiber bragg gratings, Opt Express 23 (2015) 6058, https://doi.org/10.1364/OE.23.006058.
[12] Y. Tang, Q. Luo, Y. Chen, K. Xu, All-silicon photoelectric biosensor on Chip based on silicon nitride waveguide with low loss, Nanomaterials 13 (2023) 914, https://doi.org/10.3390/nano13050914.
[13] Y. Esfahani Monfared, Overview of recent advances in the Design of Plasmonic Fiber-Optic Biosensors, Biosensors (basel) 10 (2020) 77, https://doi.org/10.3390/bios10070077.
[14] K.M. Mayer, J.H. Hafner, Localized Surface plasmon resonance sensors, Chem Rev 111 (2011) 3828–3857, https://doi.org/10.1021/cr100313v.
[15] L. Sansone, S. Campopiano, M. Pannico, M. Giordano, P. Musto, A. Iadicicco, Photonic bandgap influence on the SERS effect in metal-dielectric colloidal crystals optical fiber probe, Sens Actuators B Chem 345 (2021) 130149, https://doi.org/10.1016/j.snb.2021.130149.
[16] L. Pasquardini, N. Cennamo, F. Arcadio, C. Perri, A. Chiodi, G. D'agostino, L. Zeni, Immuno-SPR biosensor for the detection of Brucella abortus, Sci Rep 13 (2023) 22832, https://doi.org/10.1038/s41598-023-50344-5.
[17] M. Annunziata, F. Arcadio, A. Borriello, D. Bencivenga, A. Piccirillo, E. Stampone, L. Zeni, N. Cennamo, F. Della Ragione, L. Guida, A novel plasmonic optical-fiber-based point-of-care test for periodontal MIP-1α detection, Iscience 26 (2023) 108539, https://doi.org/10.1016/j.isci.2023.108539.
[18] X. Liu, S. Soares, L. Silva, A.J. Fernandes, R. Singh, B. Zhang, S. Kumar, C. Marques, SFFO Cortisol biosensor: highly sensitive S-flex fiber optic plasmonic biosensor for label-free Cortisol detection, IEEE Sens J 24 (2024) 1494–1501, https://doi.org/10.1109/JSEN.2023.3336414.
[19] S. Jain, K. Choudhary, A. Kumar, C. Marques, S. Kumar, (Invited paper) PCF-based plasmonic sensor for the detection of cervical and skin cancer cell, Results in Optics 14 (2024) 100589, https://doi.org/10.1016/j.rio.2023.100589.
[20] C. Cereser, S. Boget, P. Parvaz, A. Revol, Thiram-induced cytotoxicity is accompanied by a rapid and drastic oxidation of reduced glutathione with consecutive lipid peroxidation and cell death, Toxicology 163 (2001) 153–162, https://doi.org/10.1016/S0300-483X(01)00401-2.
[21] L. Zhang, C. Jiang, Z. Zhang, Graphene oxide embedded sandwich nanostructures for enhanced raman readout and their applications in pesticide monitoring, Nanoscale 5 (2013) 3773, https://doi.org/10.1039/c3nr00631j.
[22] K. Saha, S.S. Agasti, C. Kim, X. Li, V.M. Rotello, Gold Nanoparticles in chemical and biological sensing, Chem Rev 112 (2012) 2739–2779, https://doi.org/10.1021/cr2001178.
[23] P.K. Jain, K.S. Lee, I.H. El-Sayed, M.A. El-Sayed, Calculated absorption and scattering properties of gold Nanoparticles of different size, shape, and composition: applications in biological imaging and biomedicine, J Phys Chem B 110 (2006) 7238–7248, https://doi.org/10.1021/jp057170o.
[24] S. Zeng, K.-T. Yong, I. Roy, X.-Q. Dinh, X. Yu, F. Luan, A review on functionalized gold Nanoparticles for biosensing applications, Plasmonics 6 (2011) 491–506, https://doi.org/10.1007/s11468-011-9228-1.
[25] V.T. Huong, N.T.T. Phuong, N.T. Tai, N.T. An, V.D. Lam, D.H. Manh, T.T.K. Chi, N. X.D. Mai, V.-D. Phung, N.H.T. Tran, Gold Nanoparticles modified a multimode clad-free fiber for ultrasensitive detection of bovine serum albumin, J Nanomater 2021 (2021) 1–6, https://doi.org/10.1155/2021/5530709.
[26] S. Kumar, Z. Guo, R. Singh, Q. Wang, B. Zhang, S. Cheng, F.-Z. Liu, C. Marques, B. K. Kaushik, R. Jha, MoS_2 functionalized multicore fiber probes for selective detection of *shigella* bacteria based on localized plasmon, J. Lightwave Technol. 39 (2021) 4069–4081, https://doi.org/10.1109/JLT.2020.3036610.
[27] P.Q.T. Do, V.T. Huong, N.T.T. Phuong, T.-H. Nguyen, H.K.T. Ta, H. Ju, T.B. Phan, V.-D. Phung, K.T.L. Trinh, N.H.T. Tran, The highly sensitive determination of serotonin by using gold nanoparticles (au NPs) with a localized surface plasmon resonance (LSPR) absorption wavelength in the visible region, RSC Adv 10 (2020) 30858–30869, https://doi.org/10.1039/D0RA05271J.
[28] L.-K. Chau, Y.-F. Lin, S.-F. Cheng, T.-J. Lin, Fiber-optic chemical and biochemical probes based on localized surface plasmon resonance, Sens Actuators B Chem 113 (2006) 100–105, https://doi.org/10.1016/j.snb.2005.02.034.
[29] J.R.L. Guerreiro, M. Frederiksen, V.E. Bochenkov, V. De Freitas, M.G. Ferreira Sales, D.S. Sutherland, Multifunctional Biosensor Based on Localized Surface Plasmon Resonance for Monitoring Small Molecule–Protein Interaction, ACS Nano 8 (2014) 7958–7967. Doi: 10.1021/nn501962y.
[30] Y. Wang, J. Zhou, J. Li, Construction of plasmonic Nano-biosensor-based Devices for point-of-Care testing, Small Methods 1 (2017), https://doi.org/10.1002/smtd.201700197.
[31] K.A. Willets, R.P. Van Duyne, Localized Surface plasmon resonance spectroscopy and sensing, Annu Rev Phys Chem 58 (2007) 267–297, https://doi.org/10.1146/annurev.physchem.58.032806.104607.
[32] S. Walia, R.K. Sharma, B.S. Parmar, Isolation and simultaneous LC analysis of thiram and its less toxic transformation product in DS formulation, Bull Environ Contam Toxicol 83 (2009) 363–368, https://doi.org/10.1007/s00128-009-9754-0.
[33] N. Alizadeh, H. Kalhor, A. Karimi, Determination of thiram residues in canola seeds, water and soil samples using solid-phase microextraction with polypyrrole film followed by ion mobility spectrometer, Int J Environ Anal Chem 95 (2015) 57–66, https://doi.org/10.1080/03067319.2014.983496.
[34] S. Rastegarzadeh, Sh. Abdali, Colorimetric determination of thiram based on formation of gold nanoparticles using ascorbic acid, Talanta 104 (2013) 22–26, https://doi.org/10.1016/j.talanta.2012.11.023.
[35] K.M. Giannoulis, D.L. Giokas, G.Z. Tsogas, A.G. Vlessidis, Ligand-free gold nanoparticles as colorimetric probes for the non-destructive determination of total dithiocarbamate pesticides after solid phase extraction, Talanta 119 (2014) 276–283, https://doi.org/10.1016/j.talanta.2013.10.063.
[36] K. Liu, Y. Jin, Y. Wu, J. Liang, Simple and rapid colorimetric visualization of tetramethylthiuram disulfide (thiram) sensing based on anti-aggregation of gold nanoparticles, Food Chem 384 (2022) 132223, https://doi.org/10.1016/j.foodchem.2022.132223.
[37] J.V. Rohit, S.K. Kailasa, Cyclen dithiocarbamate-functionalized silver nanoparticles as a probe for colorimetric sensing of thiram and paraquat pesticides via host–guest chemistry, J. Nanopart. Res. 16 (2014) 2585, https://doi.org/10.1007/s11051-014-2585-x.
[38] V.-T. Hoang, N.X. Dinh, N. Le Nhat Trang, N.T. Khi, N. Van Quy, P.A. Tuan, D. Q. Tri, L.H. Thang, T.Q. Huy, A.-t., Le, functionalized silver nanoparticles-based efficient colorimetric platform: effects of surface capping agents on the sensing

response of thiram pesticide in environmental water samples, Mater Res Bull 139 (2021) 111278, https://doi.org/10.1016/j.materresbull.2021.111278.
[39] N.T. Anh, N.X. Dinh, H. Van Tuan, T.H. Thuan, L.M. Tung, V.P. Le, D.Q. Tri, A.-T. Le, Cost-effective tween 80-capped copper Nanoparticles for ultrasensitive colorimetric detection of thiram pesticide in environmental water samples, J Nanomater 2021 (2021) 1–10, https://doi.org/10.1155/2021/5513401.
[40] L. Kong, M. Huang, J. Chen, M. Lin, *In situ* detection of thiram in fruits and vegetables by colorimetry/surface-enhanced Raman spectroscopy, Laser Phys. 30 (2020) 065602, https://doi.org/10.1088/1555-6611/ab881e.
[41] G. Barbillon, O. Graniel, M. Bechelany, Assembled Au/ZnO Nano-urchins for SERS sensing of the pesticide thiram, Nanomaterials 11 (2021) 2174, https://doi.org/10.3390/nano11092174.
[42] A.E.F. Oliveira, A.C. Pereira, M.A.C. Resende, L.F. Ferreira, Gold Nanoparticles: a didactic step-by-step of the synthesis using the Turkevich method, mechanisms, and Characterizations, Analytica 4 (2023) 250–263, https://doi.org/10.3390/analytica4020020.
[43] P.N. Njoki, I.-I.-S. Lim, D. Mott, H.-Y. Park, B. Khan, S. Mishra, R. Sujakumar, J. Luo, C.-J. Zhong, Size Correlation of optical and spectroscopic properties for gold nanoparticles, The Journal of Physical Chemistry C 111 (2007) 14664–14669, https://doi.org/10.1021/jp074902z.
[44] K. Xu, Silicon electro-optic micro-modulator fabricated in standard CMOS technology as components for all silicon monolithic integrated optoelectronic systems *, J. Micromech. Microeng. 31 (2021) 054001, https://doi.org/10.1088/1361-6439/abf333.
[45] L. Litti, M. Meneghetti, Predictions on the SERS enhancement factor of gold nanosphere aggregate samples, PCCP 21 (2019) 15515–15522, https://doi.org/10.1039/C9CP02015B.
[46] H. Lei, S. Zhu, C. Liu, W. Zhang, C. Chen, H. Yan, Constructing the au nanoparticle multimer on optical fiber end face to enhance the signal of localized surface plasmon resonance biosensors: a case study for deoxynivalenol detection, Sens. Actuat. B Chem. 380 (2023) 133380, https://doi.org/10.1016/j.snb.2023.133380.
[47] N. Nath, A. Chilkoti, Label-free biosensing by Surface plasmon resonance of Nanoparticles on glass: optimization of Nanoparticle size, Anal. Chem. 76 (2004) 5370–5378, https://doi.org/10.1021/ac049741z.
[48] V. Semwal, O.R. Jensen, O. Bang, J. Janting, Investigation of performance Parameters of spherical gold Nanoparticles in localized Surface plasmon resonance biosensing, Micromachines (basel) 14 (2023) 1717, https://doi.org/10.3390/mi14091717.
[49] M. Sypabekova, A. Hagemann, D. Rho, S. Kim, Review: 3-aminopropyltriethoxysilane (APTES) deposition methods on oxide Surfaces in solution and vapor phases for biosensing applications, Biosensors (basel) 13 (2022) 36, https://doi.org/10.3390/bios13010036.
[50] Y. Lin, Y. Zou, Y. Mo, J. Guo, R.G. Lindquist, E-beam patterned gold nanodot arrays on optical fiber tips for localized Surface plasmon resonance biochemical sensing, Sensors 10 (2010) 9397–9406, https://doi.org/10.3390/s101009397.
[51] Y. Zhang, L. Ding, J. Zhao, X. Jiang, F. Ma, Localized Surface plasmon resonance-based fiber optic biosensor for acetylcholine detection, IEEE Sens. J. 23 (2023) 25987–25995, https://doi.org/10.1109/JSEN.2023.3304619.
[52] H. Parham, N. Pourreza, F. Marahel, Determination of thiram using gold nanoparticles and resonance rayleigh scattering method, Talanta 141 (2015) 143–149, https://doi.org/10.1016/j.talanta.2015.03.061.
[53] F. Esposito, L. Sansone, A. Srivastava, F. Baldini, S. Campopiano, F. Chiavaioli, M. Giordano, A. Giannetti, A. Iadicicco, Long period grating in double cladding fiber coated with graphene oxide as high-performance optical platform for biosensing, Biosens. Bioelectron. 172 (2021) 112747, https://doi.org/10.1016/j.bios.2020.112747.
[54] R.A. Dudley, P. Edwards, R.P. Ekins, D.J. Finney, I.G. McKenzie, G.M. Raab, D. Rodbard, R.P. Rodgers, Guidelines for immunoassay data processing, Clin. Chem. 31 (1985) 1264–1271, https://doi.org/10.1093/clinchem/31.8.1264.
[55] F. Chiavaioli, C. Gouveia, P. Jorge, F. Baldini, Towards a uniform metrological assessment of grating-based optical fiber sensors: from Refractometers to biosensors, Biosensors (basel) 7 (2017) 23, https://doi.org/10.3390/bios7020023.
[56] B.N. Khlebtsov, V.A. Khanadeev, E.V. Panfilova, D.N. Bratashov, N.G. Khlebtsov, Gold nanoisland films as reproducible SERS substrates for highly sensitive detection of fungicides, ACS Appl. Mater. Interfaces 7 (2015) 6518–6529, https://doi.org/10.1021/acsami.5b01652.
[57] Y. Yu, P. Zeng, C. Yang, J. Gong, R. Liang, Q. Ou, S. Zhang, Gold-nanorod-coated Capillaries for the SERS-based detection of thiram, ACS Appl. Nano Mater. 2 (2019) 598–606, https://doi.org/10.1021/acsanm.8b02075.
[58] S. Asgari, L. Sun, J. Lin, Z. Weng, G. Wu, Y. Zhang, M. Lin, Nanofibrillar cellulose/au@ag nanoparticle nanocomposite as a SERS substrate for detection of paraquat and thiram in lettuce, Microchim. Acta 187 (2020) 390, https://doi.org/10.1007/s00604-020-04358-9.
[59] X. He, S. Yang, T. Xu, Y. Song, X. Zhang, Microdroplet-captured tapes for rapid sampling and SERS detection of food contaminants, Biosens. Bioelectron. 152 (2020) 112013, https://doi.org/10.1016/j.bios.2020.112013.
[60] A. Peruga, S. Grimalt, F.J. López, J.V. Sancho, F. Hernández, Optimisation and validation of a specific analytical method for the determination of thiram residues in fruits and vegetables by LC–MS/MS, Food Chem. 135 (2012) 186–192, https://doi.org/10.1016/j.foodchem.2012.04.064.
[61] R.K. Saini, A.K. Sharma, A. Agarwal, R. Prajesh, Label-free detection of thiram pesticide on flexible SERS-active substrate, Mater. Chem. Phys. 295 (2023) 127088, https://doi.org/10.1016/j.matchemphys.2022.127088.